energies

MDPI

Article

Role of TiO_2 Phase Composition Tuned by LiOH on The Electrochemical Performance of Dual-Phase $Li_4Ti_5O_{12}$-TiO_2 Microrod as an Anode for Lithium-Ion Battery

Lukman Noerochim [1], Wahyu Caesarendra [2], Abdulloh Habib [1], Widyastuti [1], Suwarno [3], Yatim Lailun Ni'mah [4], Achmad Subhan [5], Bambang Prihandoko [5] and Buyung Kosasih [6,*]

1 Department of Materials and Metallurgical Engineering, Sepuluh Nopember Institute of Technology, Surabaya 60111, Indonesia; lukman@mat-eng.its.ac.id (L.N.); abdullohhabib57@gmail.com (A.H.); wiwidmaterial@gmail.com (W.)
2 Faculty of Integrated Technologies, Universiti Brunei Darussalam, Jalan Tungku Link BE1410, Brunei Darussalam; wahyu.caesarendra@ubd.edu.bn
3 Department of Mechanical Engineering, Sepuluh Nopember Institute of Technology, Surabaya 60111, Indonesia; warno@me.its.ac.id
4 Department of Chemistry, Sepuluh Nopember Institute of Technology, Surabaya 60111, Indonesia; yatimnikmah@gmail.com
5 Research Center of Physics, Indonesian Institute of Science, Serpong 15314, Indonesia; achmad.subhan@lipi.go.id (A.S.); bambang.prihandoko@lipi.go.id (B.P.)
6 School of Mechanical, Materials and Mechatronics Engineering, University of Wollongong, Wollongong 2522, Australia
* Correspondence: buyung@uow.edu.au

Received: 15 September 2020; Accepted: 2 October 2020; Published: 9 October 2020

Abstract: In this study, a dual-phase $Li_4Ti_5O_{12}$-TiO_2 microrod was successfully prepared using a modified hydrothermal method and calcination process. The stoichiometry of LiOH as precursor was varied at mol ratio of 0.9, 1.1, and 1.3, to obtain the appropriate phase composition between TiO_2 and $Li_4Ti_5O_{12}$. Results show that TiO_2 content has an important role in increasing the specific capacity of electrodes. The refinement of X-ray diffraction patterns by Rietveld analysis confirm that increasing the LiOH stoichiometry suppresses the TiO_2 phase. In the scanning electron microscopy images, the microrod morphology was formed after calcination with diameter sizes ranging from 142.34 to 260.62 nm and microrod lengths ranging from 5.03–7.37 μm. The 0.9 LiOH sample shows a prominent electrochemical performance with the largest specific capacity of 162.72 mAh/g and 98.75% retention capacity achieved at a rate capability test of 1 C. This finding can be attributed to the appropriate amount of TiO_2 that induced the smaller crystallite size, and lower charge transfer resistance, enhancing the lithium-ion insertion/extraction process and faster diffusion kinetics.

Keywords: hydrothermal; $Li_4Ti_5O_{12}$-TiO_2; microrod; TiO_2 rutile; lithium-ion battery

1. Introduction

With increasing interest and demand for electric cars, large power portable electrical equipment and Internet of thing (IoT) devices, massive research has been carried out to obtain secondary batteries that have a long cycle life, fast recharging, and high energy density. Lithium-ion batteries have demonstrated that they are the best candidate for these applications because they have large energy densities and an extraordinary cycle life [1–3]. However, lithium-ion batteries are not considered commercially viable for large-power application due to their rate capacity performance, cycle stability,

and low operating safety [4,5]. They are closely related to graphite as commercialized anode materials which has a low Li^+ diffusion coefficient, large volume expansion (about 9% during the battery operation process), and a safety problem due to the growth of lithium dendrites in the graphite surface when operating at a high current density [6].

Massive research has been carried out to find alternatives to graphite. $Li_4Ti_5O_{12}$ (LTO) is considered a suitable alternative to graphite and has an exceptional cycle and reversibility performance during insertion/extraction processes where the Li^+ insertion potential of LTO is very flat (approximately 1.55 V vs. Li^+/Li) [7]. It is higher than the electrolyte reduction potential which can prevent the formation of solid electrolyte interface (SEI) films, thus reducing the potential [8,9]. LTO is also known as "a zero-strain" material [10,11]. It is chemically compatible with electrolytes and has a fast phase transformation [12]. However, LTO has a low ionic and electronic conductivity coefficient [13,14]. The poor conductivity of LTO has a significant effect on the low performance rate capability and electrode polarization during charging/discharging process in large current densities, which results in decreased capacity and cycle stability. Furthermore, the theoretical specific capacity of LTO (175 mAh/g) is considered small and reduces the total energy in a battery [15]. To enhance the electrochemical performance of LTO, a number of strategies have been conducted including reduction to nanostructure [16,17], heteroatom doping [18,19], morphological control [20,21], surface modification [22,23], and coating with conductive materials [24,25].

The development of dual-phase LTO-TiO_2 [26,27], rather than the single-phase use of LTO or TiO_2 itself, results in an increase in electronic and ionic conductivity. Consequently, the increase in electrochemical performance is associated with an increase in grain boundary density in the presence of dual-phase LTO-TiO_2, rather than in each single phase, which serves to provide enough channels for electrons and reduces the energy barrier for the diffusion of lithium ions in particles [28]. In addition, the presence of TiO_2 rutile, with a theoretical capacity of 335 mAh/g, has a significant contribution to the enhancement of the specific capacity of the composite material [29]. Although, there are wide studies on the dual phase LTO-TiO_2 [30,31], discussions on the exact amount compositions of TiO_2 phase in the LTO-TiO_2 which will improve the capacity of electrodes, are still rare.

In this study, the preparation of a dual-phase LTO-TiO_2 microrod was carried out using a modified hydrothermal method and calcination process. The stoichiometry of LiOH as one of the precursors was varied to obtain the appropriate TiO_2 composition in the LTO-TiO_2 microrod to optimize its electrochemical performance. The tuning process of the dual-phase by variation of LiOH and calcination at 800 °C is one method to obtain LTO-TiO_2 rutile with the microrod morphology. The optimal composition of rutile TiO_2 induced the high density of grain boundary enhancing the electron transport for better electrochemical performance of dual-phase LTO-TiO_2 by reaching discharge capacity of 160.70 mAh/g at 1 C. This result might be useful for better understanding how the mechanism on lithium-ion batteries, especially for the type of electrode with dual-phase.

2. Materials and Methods

2.1. Preparation of LTO-TiO_2

First, 2.8 g of TiO_2 powder was mixed and stirred with 25 mL of 10 M NaOH solution to form a suspension by magnetic stirrer. The suspension was placed into a Teflon-lined stainless autoclave, and then heated in a muffle furnace for 24 h at a temperature of 200 °C. The precipitate Na-Ti-O, which is the result of the hydrothermal process, was washed using distilled water and dried for 24 h. Then, the ion-exchange process was carried out by mixing as-prepared Na-Ti-O powder with 1 M HCl solution through stirring for 12 h by magnetic stirrer. This process aims to obtain H-Ti-O precipitate by replacing Na^+ ions in Na-Ti-O with H^+ ion and this precipitate was washed with distilled water and dried. The H-Ti-O precipitate was mixed with 0.6 M LiOH with varying stoichiometry ratios of 0.9, 1.1, and 1.3, and stirred for 10 h. The prepared solution was dried and calcined at a temperature of 800 °C for 4 h in an air atmospheric to obtain the dual-phase LTO-TiO_2 microrod.

2.2. Material Characterization

To evaluate the composition of the phases formed in all three samples, an XRD test was performed using PANAnalythical instruments at an angle range of 10–90° and CuKα wavelength of 1.54056 Å. The morphology of Na-Ti-O and LTO-TiO_2 was observed by scanning electron microscopy (SEM) using Phillips-Inspect S50 (FEI Technologies Inc., Oregon, OR, USA) with 20 KV energy.

2.3. Electrochemical Measurement

Electrochemical testing was carried out on a half-cell battery that is fabricated in a glove box filled with argon gas. The working electrode is in the form of an active material of LTO-TiO_2 microrod (85 wt.%), acetylene black (10 wt.%), and polyvinylidene fluoride (5 wt.%) which has been coated in the current collector of a cupper foil, whereas Li metal was used as the counter and reference electrodes. Li metal and working electrode were separated by a separator of polypropylene (Celgard). Electrolytes used were 1 M $LiPF_6$ in ethylene carbonate and ethyl methyl carbonate solvents with a volume ratio of 3:7. A cyclic voltammetry test was carried out using the CorrTest CS350 electrochemical workstation (Wuhan Corrtest Instruments Corp., Ltd, Hubei, China) with a potential window of 1.0–3.0 V vs. Li/Li^+ at a scan rate of 0.1 mV/s. Meanwhile, a charge/discharge test was carried out using the Neware Coin Cell Battery Tester CT-4008 instrument (Neware Technology Limited, Shenzhen, China) with varying C-rates from 0.4 C to 5 C. An electrochemical impedance spectroscopy (EIS) test was performed to measure the electrolyte and charge transfer resistance using CorrTest CS350 electrochemical workstation with a frequency range of 0.1–100,000 Hz.

3. Results

Figure 1 shows the XRD pattern of the three calcined samples with different LiOH stoichiometry variations. The three patterns clearly correspond well to the diffraction pattern possessed by $Li_4Ti_5O_{12}$ with cubic spinel (JCPDS 00-049-0207) and TiO_2 rutile (JCPDS 00-021-1276) [32]. In addition, the intensity of the LTO diffraction peaks is higher than diffraction peak of TiO_2, which increases the LiOH composition in the samples.

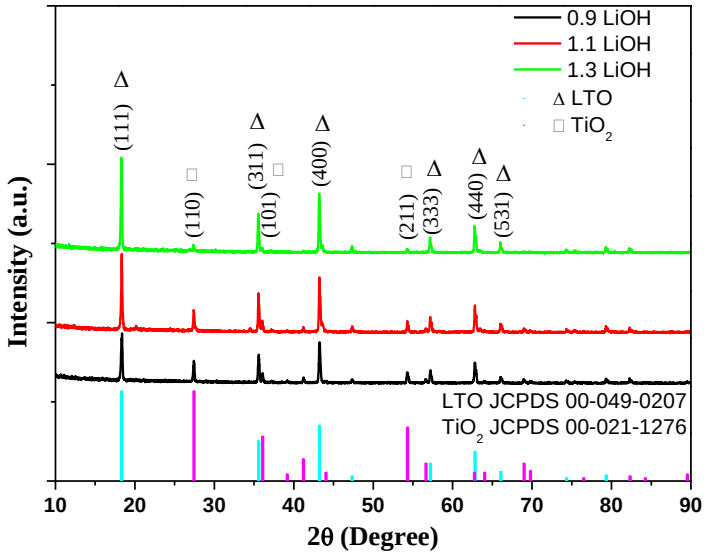

(**a**)

Figure 1. *Cont.*

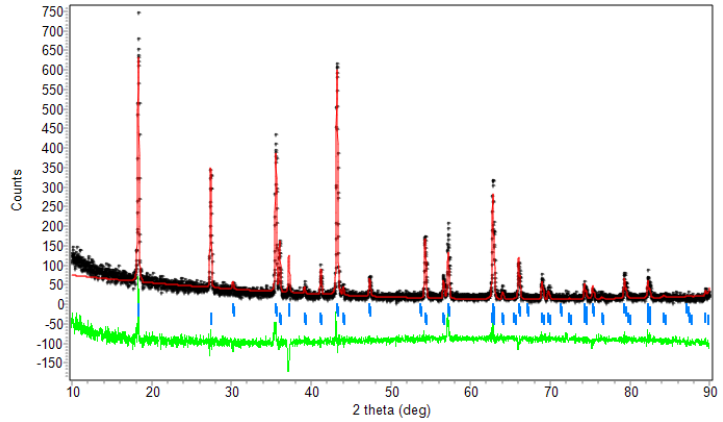

(**b**)

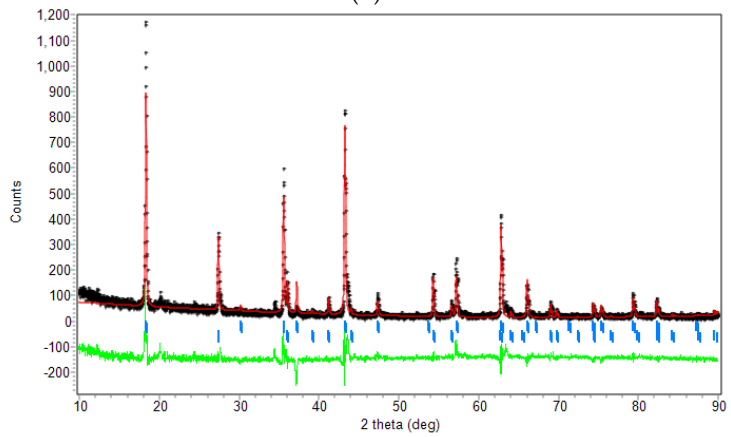

(**c**)

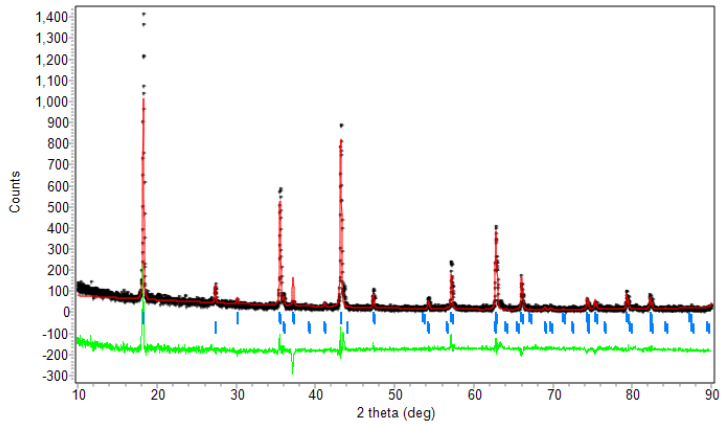

(**d**)

Figure 1. (**a**) Diffraction patterns of LTO-TiO_2 with different LiOH stoichiometry variations, (**b**) Rietveld refinement of 0.9, (**c**) 1.5, and (**d**) 2.0 LiOH samples.

By using the Scherrer formula based on peaks (111) and (110) for LTO and TiO_2, respectively, the 0.9 LiOH sample has the smallest size crystallite, both for LTO and TiO_2. As shown in Table 1, the crystallite size of 0.9 LiOH for LTO and TiO_2 is equal to 40.0 and 49.0 nm, respectively.

Table 1. Calculation of crystallite size using the Scherer formula.

Sample	Phase	Full Width at Half Maximum (FWHM) (°)	2θ (°)	Crystallite Size (nm)
0.9 LiOH	LTO	0.201	18.399	40.0
	TiO_2	0.167	27.418	49.0
1.1 LiOH	LTO	0.117	18.335	68.8
	TiO_2	0.067	27.399	52.0
1.3 LiOH	LTO	0.151	18.297	53.3
	TiO_2	0.134	27.383	61.0

Furthermore, to determine the effect of LiOH stoichiometry on the composition TiO_2 and LTO in the dual-phase LTO-TiO_2, the quantitative analysis was performed using the Rietveld refinement analysis of XRD pattern by Reitica (Figure 1b–d). Various refined-structural parameters, such as R_p (profile fitting), R_{wp} (weighted profile), and χ^2 (goodness of fit factor), obtained from the Rietveld refinement are presented in Table 2. The low values of χ^2 suggest that the samples have good quality of refinements. The results also show that increasing the LiOH stoichiometry suppresses the TiO_2 phase, from 25.90 wt.% in 0.9 LiOH to only 6.10 wt.% in 1.3 LiOH, as shown in Table 2.

Table 2. Results of phase composition and structural parameters obtained from the Rietveld analysis.

Sample	Phase	Composition (wt.%)	R_p	R_{wp}	χ^2
0.9 LiOH	LTO	74.10	18.55	25.38	2.67
	TiO_2	25.90			
1.1 LiOH	LTO	82.04	20.15	26.71	3.25
	TiO_2	17.96			
1.3 LiOH	LTO	93.90	19.87	26.94	3.24
	TiO_2	6.10			

Figure 2a shows the SEM image of Na-Ti-O as product of the hydrothermal process. The hydrothermal process is the determinant process of the nanowire formation in accordance with what was previously reported [33]. However, in this study, TiO_2 powder was used instead of titanium sheets. The resulting nanowire has dimensions approximately 0.142–0.260 μm and 5.003–7.377 μm for the diameter and length, respectively. Figure 2b–d shows SEM images of LTO-TiO_2 calcined at 800 °C for 0.9, 1.1, and 1.3 LiOH, respectively.

It is observed that the morphology of nanowire owned by Na-Ti-O was successfully transform into microrod after calcination. Of note, changes in length dimensions became smaller, as shown in Table 3. Such a change could be the result of a physical treatment, such as the grain growth process, which results in a reduction in the dimensions of the nanowire length.

Figure 3 shows the cyclic voltammogram (CV) of the three samples of LTO-TiO_2 at 1.0–3.0 V (vs. Li/Li^+) with a scan rate of 0.1 mV/s. As shown in Figure 3, all the three samples have two pairs redox peak relating to the intercalation and de-intercalation of lithium ions in LTO-TiO_2. This finding is consistent in a previous report that LTO-TiO_2 rutile has a pair of redox peaks observed in the intercalation/de-intercalation process [32,33]. As shown in Figure 3, the cathodic peaks are located around 1.42 V and 1.71 V for all three samples of LTO-TiO_2 where Li ions are intercalated into and TiO_2. Meanwhile, the anodic peaks are located around 1.66 V and 2.12 V, where Li ions are de-intercalated from LTO and TiO_2. Anode LTO-TiO_2 undergoes two reactions during the discharge process, first, Li ions are intercalated into TiO_2 at a voltage of about 1.71 V, and then below 1.71 V the anode changes to Li_xTiO_2 and $Li_4Ti_5O_{12}$. Second, during the process of decreasing the discharge voltage, Li ions are intercalated into $Li_4Ti_5O_{12}$. After the complete discharge process, the anode consists of Li_xTiO_2 and $Li_7Ti_5O_{12}$. Next, during the charge process, Li ions are extracted from $Li_7Ti_5O_{12}$ at a voltage of about

1.66 V. Above a voltage of 1.66 V the anode consists of Li_xTiO_2 and $Li_4Ti_5O_{12}$. As the voltage increases during the charge process, Li ions are extracted from Li_xTiO_2. It should be noted that the Li_xTiO_2 phase is always present during the insertion/extraction process of Li-ions into LTO-TiO_2.

The charge/discharge curve at different C-rates is shown in Figure 4. Figure 4 shows that the 0.9 LiOH sample has the highest specific discharge capacity at 0.4 C (162.72 mAh/g) followed by the 1.1 and 1.3 LiOH samples at 159.58 mAh/g and 150.80 mAh/g, respectively. Moreover, all samples except for the 1.3 LiOH sample have a plateau of a C-rate of 5 C. In addition, with the increase in the C-rate, the polarization potential gradually increases in all the three samples. Furthermore, the 0.9 LiOH sample can maintain its capacity without experiencing a significant deterioration of C-rate up to 2 C, whereas the 1.3 LiOH sample shows a large decrease in specific capacity at a C-rate of 5 C. These results could be attributed to the conductivity of each sample, where the 0.9 and 1.1 LiOH samples have low polarization and good kinetics reaction than the 1.3 LiOH sample [34].

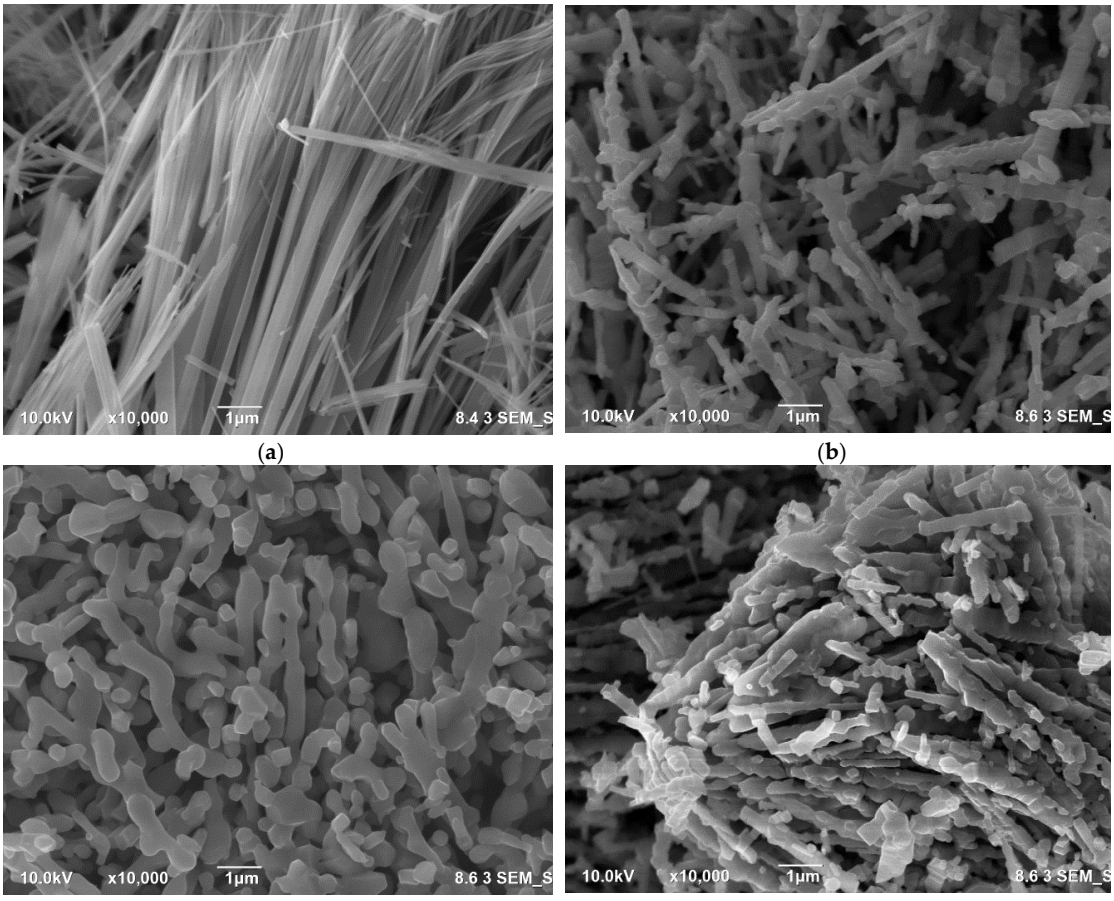

Figure 2. (**a**) SEM images of the morphology of Na-Ti-O and LTO-TiO_2 samples with the stoichiometry of the (**b**) 0.9, (**c**) 1.1, and (**d**) 1.3 LiOH samples.

Table 3. Comparison of size and dimension between Na-Ti-O and LTO-TiO_2.

Sample	Diameter (μm)	Length (μm)
Na-Ti-O	0.142–0.260	5.003–7.377
LTO-TiO_2 (0.9 LiOH)	0.110–0.125	1.073–2.481
LTO-TiO_2 (1.1 LiOH)	0.234–0.429	4.390–4.660
LTO-TiO_2 (1.3 LiOH)	0.112–0.298	3.603–2.505

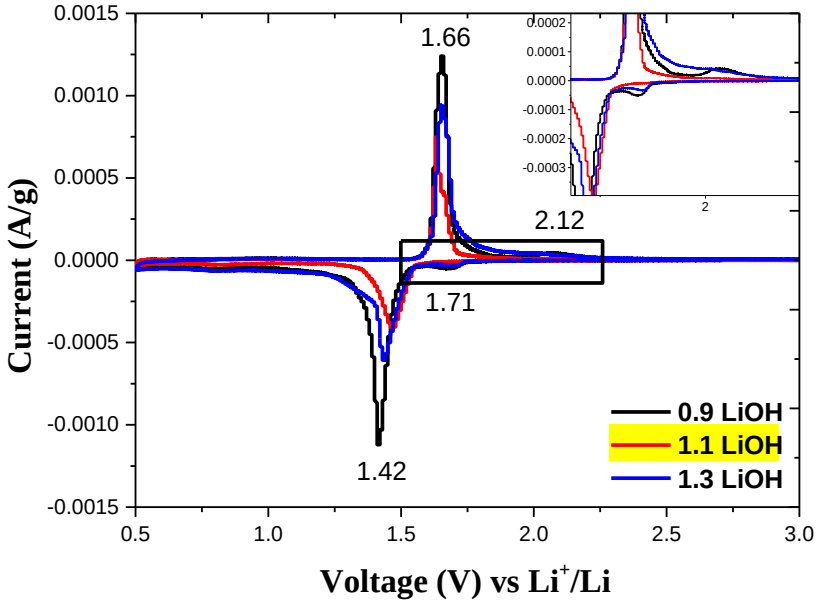

Figure 3. Cyclic voltammogram of the LTO-TiO_2 samples with different LiOH stoichiometry with insert graph for higher magnification of the rectangle mark.

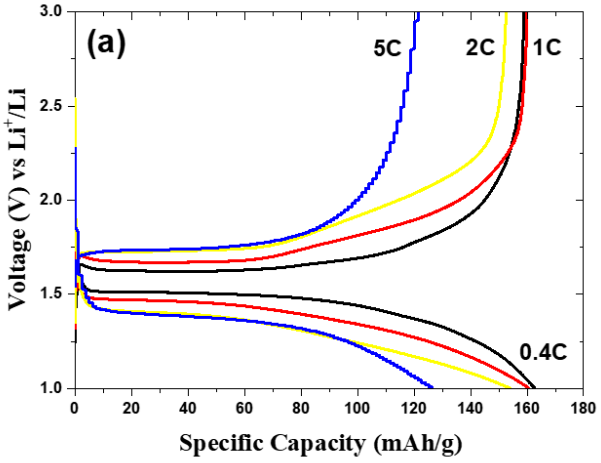

(**a**)

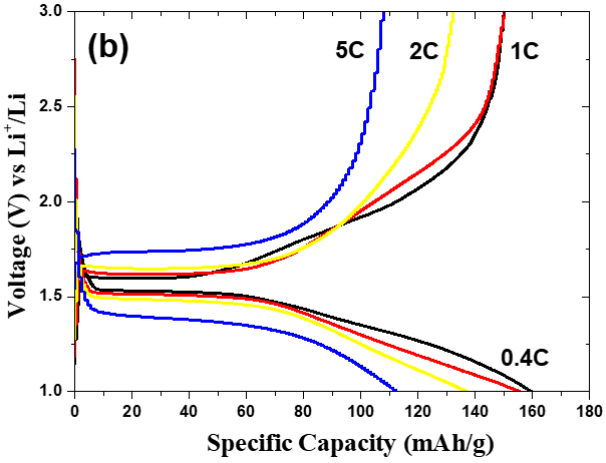

(**b**)

Figure 4. *Cont.*

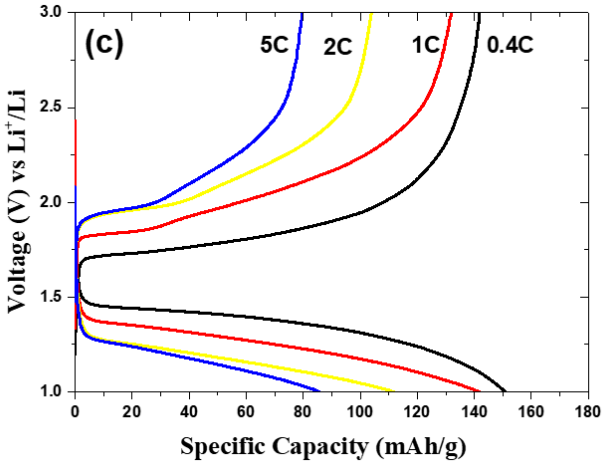

(**c**)

Figure 4. Charge/discharge curve of LTO-TiO_2 at four different C-rates for the (**a**) 0.9, (**b**) 1.1, and (**c**) 1.3 LiOH samples.

To identify the performance rate capability of LTO-TiO_2 with various LiOH stoichiometry variations, a charge/discharge test was carried out at 1.0–3.0 V (vs. Li/Li^+) with C-rates of 0.4 C, 1 C, 2 C, and 5 C, and back to 0.4 C as many as 10 cycles for each C-rate as shown in Figure 5a. The 0.9 LiOH sample has a superior discharge capacity with C-rates of 0.4 C, 1 C, 2 C, and 5 C at 162.72 mAh/g, 160.70 mAh/g, 154.01 mAh/g, and 126.37 mAh/g, respectively. Meanwhile, the 1.3 LiOH sample has the inferior performance rate with discharge capacities of 150.80 mAh/g, 141.75 mAh/g, 111.75 mAh/g, and 85.67 mAh/g at C-rates of 0.4 C, 1 C, 2 C, and 5 C, respectively. The discharge capacity of 0.9 LiOH at a rate of 1 C is slightly higher than the dual phase LTO-TiO_2 from previous studies [28] where the discharge capacity was obtained of 156 mAh/g at the same current rate. The 0.9 LiOH sample has the best stability rate after the C-rate is returned at 0.4 C followed by the 1.1 and 1.3 LiOH samples with capacity retention values of 98.91%, 93.93%, and 88.86%, respectively.

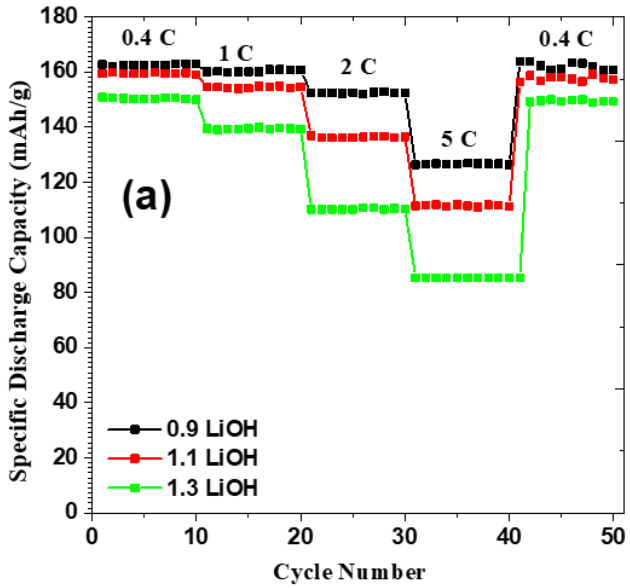

(**a**)

Figure 5. *Cont.*

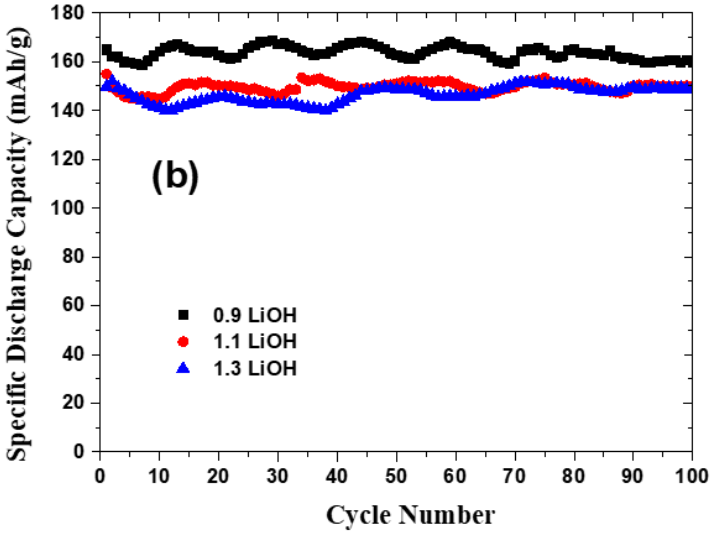

(**b**)

Figure 5. (**a**) Rate capability at 0.4 C, 1 C, 2 C, 5 C, and back to 0.4 C for the LTO-TiO_2 samples, and (**b**) cycle stability for all LTO-TiO_2 samples at 0.4 C.

To evaluate the potential cycle life, a cyclability testing was carried out at 1.0–3.0 V (vs. Li/Li^+) with 0.4 C as shown in Figure 5b. After 100 cycles, the 0.9 LiOH sample has the highest stability with discharge capacities reaching 159.73 mAh/g, which is 98.16% of the initial capacity. By contrast, the 1.1 and 1.3 LiOH samples were only able to maintain their respective capacities of 96.79% and 95.29%, which deliver specific capacities of 149.95 mAh/g and 143.63 mAh/g, respectively, in the last cycle.

To analyze the charge transfer resistance and Li^+ diffusion during the charge–discharge process, the EIS measurement was carried out and plotted as a Nyquist curve where all three LTO-TiO_2 samples show an almost identical impedance spectra pattern, which is a semicircle in the high frequency region and a slope in the lower frequency region related to the charge transfer of resistance and diffusion of lithium ions in the electrode material or commonly called Warburg diffusion, respectively [35]. Meanwhile, the intersection between the semicircle in the high frequency regions with axis Z′ is related to the electrolyte cell resistance. The curve is fitted with the equivalent circuit inserted in Figure 6a.

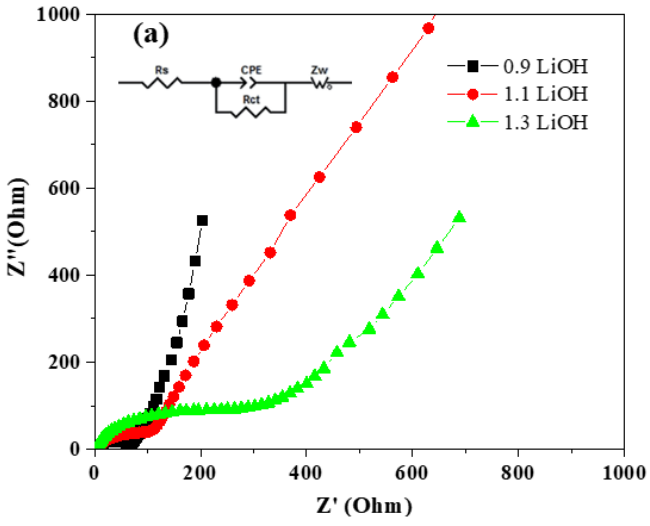

(**a**)

Figure 6. *Cont.*

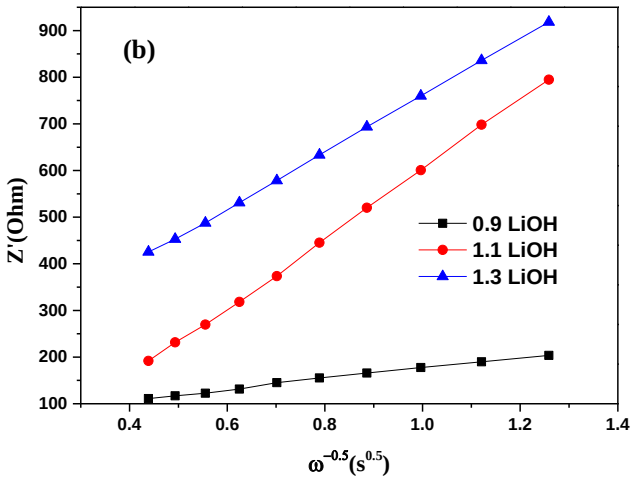

(**b**)

Figure 6. (**a**) Nyquist plot and (**b**) the relationship between Z′ and the lower angular frequencies of all LTO-TiO_2 samples.

Meanwhile, the diffusion coefficient of the lithium ion in the electrode material is determined by Equations (1) and (2). The relationship between Z′ and the lower angular is plotted in Figure 6b.

$$Z' = R_s + R_{ct} + \sigma_\omega\ \omega^{-0.5} \quad (1)$$

$$D = 0.5\left(\frac{RT}{AF^2\sigma_\omega C}\right)^2 \quad (2)$$

where Z′ is a real impedance, R_s is the electrolyte resistance, R_{ct} is the charge transfer resistance, σ_ω is the Warburg factor, ω is the angular frequency, D is the diffusion coefficient of lithium ions in the electrode material, R is the gas constant (8.314 J mol^{-1} K^{-1}), T is the absolute temperature (K), A is the surface area of the electrode (cm^2), F is the Faraday constant (96 486.33 C mol^{-1}), and C is the molar concentration of lithium ion (7.69×10^{-3} mol cm^{-3}) [21]. A summary of the EIS measurement and the diffusion coefficient of lithium ions (D) in the electrode material is shown in Table 4.

Table 4. Parameter data of the Nyquist plot from the LTO-TiO_2 samples.

Sample	R_s (Ohm)	R_{ct} (Ohm)	σ_w (Ohm $s^{-0.5}$)	D (cm^{-2} s^{-1})
0.9 LiOH	5.02	68.5	97.62	1.61×10^{-14}
1.1 LiOH	4.88	118	368.72	1.75×10^{-15}
1.3 LiOH	3.89	312	377.20	1.21×10^{-15}

The plot between conductivity and temperature (K) is expressed as an Arrhenius plot. The Arrhenius plot of the conductivity of the LTO-TiO_2 material with variations of LiOH is shown in Figure 7. In this figure, it can be seen that high conductivity occurs at high temperatures when LiOH concentrations are lower.

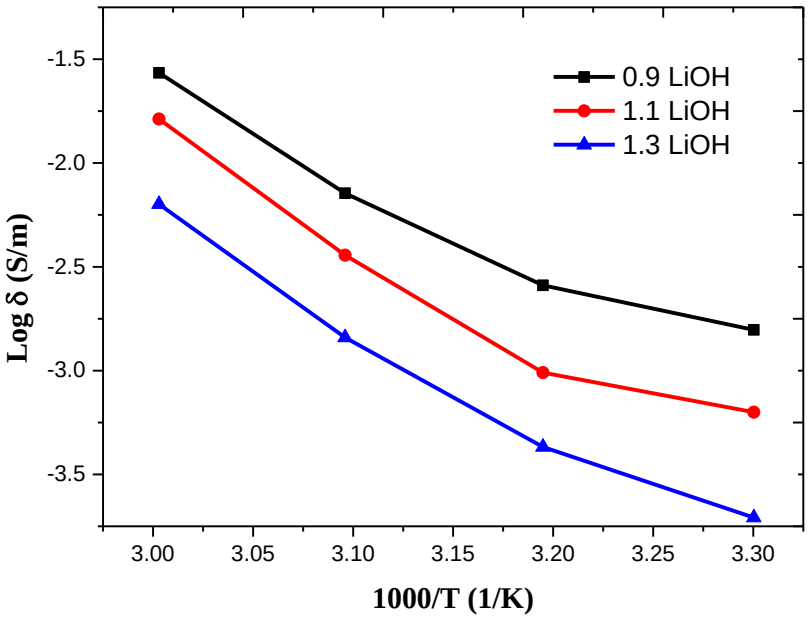

Figure 7. Temperature-dependent conductivity plots of dual-phase LTO-TiO_2 in various concentrations of LiOH.

4. Discussion

As shown in Table 1, the crystallite size of 0.9 LiOH is smaller than other LTO-TiO_2 samples. The smaller crystallite size could provide more abundant grain boundary and grain size growth inhibition when processing at high temperatures. However, compared with the results previously reported [32], the result obtained in this study were more than 10 times greater. This could be attributed to the higher calcination temperature (800 °C) compared to that reported at 600 C [32].

The crystallite size change in the 0.9 LiOH and other samples could be related to the percentage change of TiO_2 phase. It is confirmed that the lattice volume of TiO_2 phase is smaller (63.92 $Å^3$) [36] than the lattice volume of the LTO phase (582.73 $Å^3$) [37]. Therefore, when the percentage of the TiO_2 phase gets larger, it could decrease the crystallite size of LTO-TiO_2 samples (Table 1). In this case, the increasing the LiOH stoichiometry suppresses the TiO_2 phase, from 25.90 wt.% in 0.9 LiOH to only 6.10 wt.% in 1.3 LiOH, as shown in Table 2.

In the SEM images result, the dimension reduction of the LTO-TiO_2 sample generally shows the similar trend as indicated by the crystallite size. The 0.9 LiOH sample has the smallest diameter size compared to other samples, which might be correlated with the small crystallite size. Furthermore, LTO-TiO_2 has a rough surface similar to what was previously reported [33]. The rough surfaces and smaller diameters could provide greater active surface area and shorter diffusion of lithium ions, thus facilitating faster lithiation/de-lithiation process.

Redox reaction in the lithiation/de-lithiation process can be observed in the cyclic voltammetry profile curve as shown in the Figure 3. It is noticed that the Li_xTiO_2 phase is always present during the insertion/extraction process of Li-ions into LTO-TiO_2. Li_xTiO_2 is very conductive phase compared to pure TiO_2 due to the formation of a mixture of Ti^{4+}/Ti^{3+} surface oxidation states [38]. Therefore, after the Li ion is inserted into the TiO_2 phase, Li_xTiO_2 will be formed during the insertion/extraction process of Li ions in LTO-TiO_2. As the results, the electronic conductivity of LTO-TiO_2 is enhanced significantly. Moreover in the Figure 3, it is clearly observed that 0.9 LiOH sample has the highest intensity of redox peaks, indicating that the electronic conductivity during the intercalation/de-intercalation process occurs in the 0.9 LiOH higher than that of other samples.

As the result, the specific discharge capacity of the 0.9 LiOH sample is superior to that of the other samples. This could be also the highest content of the TiO_2 rutile phase in the LTO-TiO_2 electrode, as

shown in the XRD results, where TiO_2 rutile has a theoretical specific capacity of 335 mAh/g, which contributes to the specific capacity of the electrode [35]. It was also reported that the dual phase LTO-TiO_2 rutile showed the best electrochemical performance when compared to anatase TiO_2 or a mixture of anatase and rutile of TiO_2. It is attributed to the Li-ions mobility is low when Lithium is inserted into anatase TiO_2 at high lithium content ($x > 0.5$ for Li_xTiO_2) [36].

To evaluate the total resistance in the anode of 0.9 LiOH sample, the electrochemical impedance spectroscopy was performed. The Rs value is closely related to the resistance of electrolyte, and the three samples show no significant difference in values, which can be correlated with the similarity of the materials used in the three samples during the assembly process. Meanwhile, the 0.9 LiOH sample shows the smallest charge transfer resistance, whereas the 1.3 LiOH sample shows a low performance, which is equal to 68.5 Ohm and 312 Ohm, respectively. This finding suggests that low charge transfer resistance could be the reason for the good rate stability performance and retention capacity of the 0.9 LiOH sample [35]. Furthermore, the calculation results of the Li diffusion coefficient in the electrode material show that the 0.9 LiOH sample is superior compared to that of the other two samples with values of 1.61×10^{-14}, 1.75×10^{-15}, and 1.21×10^{-15} cm^{-2} s^{-1} for the 0.9, 1.1, and 1.3 LiOH samples, respectively. These results indicate that the 0.9 LiOH sample has the highest Li^+ diffusion and leads to the fastest faradic reaction. This finding could be in line with the results of the crystallite size where the 0.9 LiOH sample has the smallest crystallite size. The smaller crystallite size might be correlated with the increasing grain boundaries [28]. It is also reported that a large grain boundary interface area in the LTO-TiO_2 composites increases the electronic conductivity and structural stability [28]. In addition, the results of the dimensional measurements in the SEM images show a similar pattern, where the 0.9 LiOH sample has the smallest diameter that allows the short diffusion path of the lithium ions [28]. A large active surface has been found as one of the factors that can reduce the value of the charge transfer resistance [39]. Therefore, in this study, the appropriate amount of TiO_2 phase (approximately 25%) in the dual-phase LTO-TiO_2 would induce the smaller crystallite size and enhance the grain boundary density, which are the determinant factors of the superior electrochemical performance of the 0.9 LiOH sample.

Furthermore, the rutile TiO_2 in LTO-TiO_2 samples also has contributed to increase the conductivity. It has been reported that Li ion can intercalate to rutile TiO_2 during the initial discharge process at 1.7 V (vs. Li^+ /Li), leading to the formation process of Li_xTiO_2 [31]. The existence of Li_xTiO_2 phase is believed to enhance the total electrical conductivity due to the formation of a Ti^{3+}/Ti^{4+} mixture. A similar mechanism might be occurred with LTO-TiO_2, particularly the 0.9 LiOH sample. Where the rutile-TiO_2 redox peak at 0.9, LiOH was very prominent at the initial of the discharge curve with a slope-like profile in the potential range between 1.5 V and 2.5 V (vs Li^+/Li), which was also clearly observed in the CV curve profile. This is attributed to the rutile TiO_2 content which was higher at 0.9 LiOH compared to other samples. As a result, this leads to a higher formation of Li_xTiO_2 phase, which has implications for increasing the conductivity of the 0.9 LiOH sample.

Figure 7 shows the temperature-dependent conductivity plots of dual-phase LTO-TiO_2 in various concentrations of LiOH. It is clearly observed that the mobility of Li ions transfer in the anode material is enhanced due to the increasing number of rutile TiO_2 phases as in the 0.9 LiOH sample with 25% of rutile TiO_2 phase. It is reported in previous studies that the mobility of lithium ion in the rutile TiO_2 phase was higher than the anatase TiO_2 phase [38,40]. As the result, if the proper composition of rutile TiO_2 phase is added, it will be able to increase the conductivity of electrode. The slope of the curve on the Arrhenius plot of total conductivity shows the activation energy (Ea). By entering the value of the gradient (slope) in the linear equation to the Arrhenius equation, the respective activation energy for each material is obtained, namely, 34.68 J/mol (0.9 LiOH), 40.00 J/mol (1.1 LiOH), and 42.21 J/mol (1.3 LiOH). These results indicate a strong correlation between ionic conductivity and activation energy. It shows that high conductivity is associated with low activation energy. In this case, it shows the important role of rutile TiO_2 phase in improving the electrochemical performance of lithium-ion batteries with dual-phase LTO-TiO_2 electrodes.

5. Conclusions

A dual-phase LTO-TiO_2 microrod has been successfully synthesized using a modified hydrothermal method on stoichiometric variations of 0.9, 1.1, and 1.3 LiOH, followed by calcination at 800 °C for 4 h. The TiO_2 content in the LTO-TiO_2 products decreased with the increasing LiOH stoichiometry. In the SEM images, the 0.9 LiOH sample has the smallest diameter size and crystallite size. The 0.9 LiOH sample shows the best electrochemical performance with a specific capacity of 162.72 mAh/g and 97% capacity retention at 0.4 C after 100 cycles. It could be attributed to the appropriate amount of TiO_2 phase (around 25%) in the dual-phase LTO- TiO_2, which induces the smaller crystallite size and enhances the grain boundary density, which are the determinant factors of the superior electrochemical performance of the 0.9 LiOH sample. Therefore, the effect of TiO_2 rutile composition on LTO-TiO_2 as anode for lithium-ion batteries can be an interesting subject for further research.

Author Contributions: Conceptualization and writing—original draft, L.N.; methodology, A.S.; validation, B.P.; investigation, A.H.; resources, W.; writing—review and editing, S., Y.L.N., W.C., and B.K.; funding acquisition, L.N., W.C., and B.K. All authors have read and agreed to the published version of the manuscript.

Funding: This research was financially supported by Penelitian Dana Lokal ITS (No. 818/PKS/ITS/2020) and WCR scheme. The Article Processing Charge (APC) for the publication was provided by Dr. Wahyu Caesarendra and Dr. Buyung Kosasih.

Conflicts of Interest: The authors declare no conflict of interest.

References

1. Liu, J.; Lu, P.-J.; Liang, S.; Liu, J.; Wang, W.; Lei, M.; Tang, S.; Yang, Q. Ultrathin Li3VO4 Nanoribbon/Graphene Sandwich-Like Nanostructures with Ultrahigh Lithium Ion Storage Properties. *Nano Energy* **2015**, *12*, 709–724. [CrossRef]
2. Li, H.Z.; Yang, L.Y.; Liu, J.; Li, S.T.; Fang, L.B.; Lu, Y.K.; Yang, H.R.; Liu, S.L.; Lei, M. Improved Electrochemical Performance of Yolk-Shell Structured SnO2@void@C Porous Nanowires as Anode for Lithium and Sodium Batteries. *J. Power Sources* **2016**, *324*, 780–787. [CrossRef]
3. Yang, L.Y.; Li, H.Z.; Liu, J.; Tang, S.S.; Lu, Y.K.; Te Li, S.; Min, J.; Yan, N.; Lei, M. Li4Ti5O12 Nanosheets as High-Rate and Long-Life Anode Materials for Sodium-Ion Batteries. *J. Mater. Chem. A* **2015**, *3*, 24446–24452. [CrossRef]
4. Cao, N.; Wen, L.; Song, Z.; Meng, W.; Qin, X. Li4Ti5O12/Reduced Graphene Oxide Composite as a High-Rate Anode Material for Lithium Ion Batteries. *Electrochim. Acta* **2016**, *209*, 235–243. [CrossRef]
5. Chen, C.; Huang, Y.; Zhang, H.; Wang, X.; Li, G.; Wang, Y.; Jiao, L.; Yuan, H. Small Amount of Reduce Graphene Oxide Modified Li4Ti5O12 Nanoparticles for Ultrafast High-Power Lithium Ion Battery. *J. Power Sources* **2015**, *278*, 693–702. [CrossRef]
6. Huang, X.; Qi, X.; Boey, F.; Zhang, H. Graphene-Based Composites. *Chem. Soc. Rev.* **2012**, *41*, 666–686. [CrossRef]
7. Chen, Z.; Belharouak, I.; Sun, Y.-K.; Amine, K. Titanium-Based Anode Materials for Safe Lithium-Ion Batteries. *Adv. Funct. Mater.* **2012**, *23*, 959–969. [CrossRef]
8. Croce, F.; Appetecchi, G.B.; Persi, L.; Scrosati, B. Nanocomposite Polymer Electrolytes for Lithium Batteries. *Nature* **1998**, *394*, 456. [CrossRef]
9. Tarascon, J.-M.; Armand, M. Issues and Challenges Facing Rechargeable Lithium Batteries. *Nature* **2001**, *414*, 359. [CrossRef]
10. Yang, Y.; Qiao, B.; Yang, X.; Fang, L.; Pan, C.; Song, W.; Hou, H.; Ji, X. Lithium Titanate Tailored by Cathodically Induced Graphene for an Ultrafast Lithium Ion Battery. *Adv. Funct. Mater.* **2014**, *24*, 4349–4356. [CrossRef]
11. Kim, J.-G.; Park, M.-S.; Hwang, S.M.; Heo, Y.-U.; Liao, T.; Sun, Z.; Park, J.H.; Kim, K.J.; Jeong, G.; Kim, Y.-J.; et al. Zr4+ Doping in Li4Ti5O12 Anode for Lithium-Ion Batteries: Open Li+ Diffusion Paths through Structural Imperfection. *ChemSusChem* **2014**, *7*, 1451–1457. [CrossRef] [PubMed]
12. Pan, G.X.; Cao, F.; Zhang, Y.J. Graphene Foam Integrated with Lithium Titanate as Anode of Li Ion Batteries. *Mater. Res. Bull.* **2017**, *96*, 311–314. [CrossRef]

13. Aricò, A.S.; Bruce, P.; Scrosati, B.; Tarascon, J.-M.; van Schalkwijk, W. Nanostructured Materials for Advanced Energy Conversion and Storage Devices. *Nat. Mater.* **2005**, *4*, 366. [CrossRef] [PubMed]
14. Haetge, J.; Hartmann, P.; Brezesinski, K.; Janek, J.; Brezesinski, T. Ordered Large-Pore Mesoporous Li4Ti5O12 Spinel Thin Film Electrodes with Nanocrystalline Framework for High Rate Rechargeable Lithium Batteries: Relationships among Charge Storage, Electrical Conductivity, and Nanoscale Structure. *Chem. Mater.* **2011**, *23*, 4384–4393. [CrossRef]
15. Qian, D.; Gu, Y.; Chen, Y.; Liu, H.; Wang, J.; Zhou, H. Ultra-High Specific Capacity of Cr3+-Doped Li4Ti5O12 at 1.55 V as Anode Material for Lithium-Ion Batteries. *Mater. Lett.* **2019**, *238*, 102–106. [CrossRef]
16. Su, X.; Huang, T.; Wang, Y.; Yu, A. Synthesis and Electrochemical Performance of Nano-Sized Li4Ti5O12 Coated with Boron-Doped Carbon. *Electrochim. Acta* **2016**, *196*, 300–308. [CrossRef]
17. Noerochim, L.; Fikry, R.; Nurdiansah, H.; Purwaningsih, H.; Subhan, A.; Triwibowo, J.; Prihandoko, B. Synthesis of Dual-Phase Li4Ti5O12-TiO2 Nanowires as Anode for Lithium-Ion Battery. *Ionics* **2018**. [CrossRef]
18. Li, N.; Zhou, G.; Li, F.; Wen, L.; Cheng, H.-M. A Self-Standing and Flexible Electrode of Li4Ti5O12 Nanosheets with a N-Doped Carbon Coating for High Rate Lithium Ion Batteries. *Adv. Funct. Mater.* **2013**, *23*, 5429–5435. [CrossRef]
19. Hu, Y.; Jiang, Z.; Cai, L.; Thompson, J. Fabrication of Phosphorus-Doped Carbon-Decorated Li4Ti5O12 Anode and Its Lithium Storage Performance for Li-Ion Batteries. *Ceram. Int.* **2018**, *44*, 17544–17547. [CrossRef]
20. Li, Y.; Fu, G.; Watson, M.; Harrison, S.; Paranthaman, M.P. Monodispersed Li4Ti5O12 with Controlled Morphology as High Power Lithium Ion Battery Anodes. *ChemNanoMat* **2016**, *2*, 642–646. [CrossRef]
21. Yu, Y.; Huang, W.; Song, X.; Wang, W.; Hou, Z.; Zhao, X.; Deng, K.; Ju, H.; Sun, Y.; Zhao, Y.; et al. Thermally Reduced Graphene Paper with Fast Li Ion Diffusion for Stable Li Metal Anode. *Electrochim. Acta* **2019**, *294*, 413–422. [CrossRef]
22. Zhang, Q.; Liu, Y.; Lu, H.; Tang, D.; Ouyang, C.; Zhang, L. Ce3+-Doped Li4Ti5O12 with CeO2 Surface Modification by a Sol-Gel Method for High-Performance Lithium-Ion Batteries. *Electrochim. Acta* **2016**, *189*, 147–157. [CrossRef]
23. Dou, S.; Tao, L.; Wang, R.; El Hankari, S.; Chen, R.; Wang, S. Plasma-Assisted Synthesis and Surface Modification of Electrode Materials for Renewable Energy. *Adv. Mater.* **2018**, *30*, 1705850. [CrossRef] [PubMed]
24. Chen, C.; Xu, H.; Zhou, T.; Guo, Z.; Chen, L.; Yan, M.; Mai, L.; Hu, P.; Cheng, S.; Huang, Y.; et al. Integrated Intercalation-Based and Interfacial Sodium Storage in Graphene-Wrapped Porous Li4Ti5O12 Nanofibers Composite Aerogel. *Adv. Energy Mater.* **2016**, *6*, 1600322. [CrossRef]
25. Hui, Y.; Cao, L.; Xu, Z.; Huang, J.; Ouyang, H.; Li, J.; Hu, H. In Situ Synthesis of Core-Shell Li4Ti5O12 @ Polyaniline Composites with Enhanced Rate Performance for Lithium-Ion Battery Anodes. *J. Mater. Sci. Technol.* **2017**, *33*, 231–238. [CrossRef]
26. Rahman, M.M.; Wang, J.-Z.; Hassan, M.F.; Wexler, D.; Liu, H.K. Amorphous Carbon Coated High Grain Boundary Density Dual Phase Li4Ti5O12-TiO2: A Nanocomposite Anode Material for Li-Ion Batteries. *Adv. Energy Mater.* **2011**, *1*, 212–220. [CrossRef]
27. Zhu, G.-N.; Chen, L.; Wang, Y.-G.; Wang, C.-X.; Che, R.-C.; Xia, Y.-Y. Binary Li4Ti5O12-Li2Ti3O7 Nanocomposite as an Anode Material for Li-Ion Batteries. *Adv. Funct. Mater.* **2013**, *23*, 640–647. [CrossRef]
28. Liao, J.-Y.; Chabot, V.; Gu, M.; Wang, C.; Xiao, X.; Chen, Z. Dual Phase Li4Ti5O12–TiO2 Nanowire Arrays as Integrated Anodes for High-Rate Lithium-Ion Batteries. *Nano Energy* **2014**, *9*, 383–391. [CrossRef]
29. Gu, Y.; Zhu, Y.; Tang, Z.; Zhang, Y.; Yang, Y.; Wang, L. Design and Synthesis of Dual-Phase Li4Ti5O12–TiO2 Nanoparticles as Anode Material for Lithium Ion Batteries. *Mater. Lett.* **2014**, *131*, 118–121. [CrossRef]
30. Yi, T.-F.; Fang, Z.-K.; Xie, Y.; Zhu, Y.-R.; Yang, S.-Y. Rapid Charge—Discharge Property of Li4Ti5O12–TiO2 Nanosheet and Nanotube Composites as Anode Material for Power Lithium-Ion Batteries. *ACS Appl. Mater. Interfaces* **2014**, *6*, 20205–20213. [CrossRef]
31. Wang, Y.-Q.; Gu, L.; Guo, Y.-G.; Li, H.; He, X.-Q.; Tsukimoto, S.; Ikuhara, Y.; Wan, L.-J. Rutile-TiO2 Nanocoating for a High-Rate Li4Ti5O12 Anode of a Lithium-Ion Battery. *J. Am. Chem. Soc.* **2012**, *134*, 7874–7879. [CrossRef] [PubMed]
32. Xu, C.; Xue, L.; Zhang, W.; Fan, X.; Yan, Y.; Li, Q.; Huang, Y.; Zhang, W. Hydrothermal Synthesis of Li4Ti5O12/TiO2 Nano-Composite As High Performance Anode Material for Li-Ion Batteries. *Electrochim. Acta* **2014**, *147*, 506–512. [CrossRef]

33. Gao, L.; Wang, L.; Dai, S.; Cao, M.; Zhong, Z.; Shen, Y.; Wang, M. Li4Ti5O12-TiO2 Nanowire Arrays Constructed with Stacked Nanocrystals for High-Rate Lithium and Sodium Ion Batteries. *J. Power Sources* **2017**, *344*, 223–232. [CrossRef]
34. Liu, J.; Song, K.; van Aken, P.A.; Maier, J.; Yu, Y. Self-Supported Li4Ti5O12–C Nanotube Arrays as High-Rate and Long-Life Anode Materials for Flexible Li-Ion Batteries. *Nano Lett.* **2014**, *14*, 2597–2603. [CrossRef] [PubMed]
35. Shen, L.; Zhang, X.; Uchaker, E.; Yuan, C.; Cao, G. Li4Ti5O12 Nanoparticles Embedded in a Mesoporous Carbon Matrix as a Superior Anode Material for High Rate Lithium Ion Batteries. *Adv. Energy Mater.* **2012**, *2*, 691–698. [CrossRef]
36. Hanaor, D.A.H.; Sorrell, C.C. Review of the Anatase to Rutile Phase Transformation. *J. Mater. Sci.* **2011**, *46*, 855–874. [CrossRef]
37. Vikram Babu, B.; Vijaya Babu, K.; Tewodros Aregai, G.; Seeta Devi, L.; Madhavi Latha, B.; Sushma Reddi, M.; Samatha, K.; Veeraiah, V. Structural and Electrical Properties of Li4Ti5O12 Anode Material for Lithium-Ion Batteries. *Results Phys.* **2018**, *9*, 284–289. [CrossRef]
38. Yang, L.; Li, H.; Liu, J.; Lu, Y.; Li, S.; Min, J.; Yan, N.; Men, Z.; Lei, M. Effects of TiO2 Phase on the Performance of Li4Ti5O12 Anode for Lithium-Ion Batteries. *J. Alloys Compd.* **2016**, *689*, 812–819. [CrossRef]
39. Abraham, D.P.; Heaton, J.R.; Kang, S.-H.; Dees, D.W.; Jansen, A.N. Investigating the Low-Temperature Impedance Increase of Lithium-Ion Cells. *J. Electrochem. Soc.* **2008**, *155*, A41–A47. [CrossRef]
40. Borghols, W.J.H.; Lützenkirchen-Hecht, D.; Haake, U.; van Eck, E.R.H.; Mulder, F.M.; Wagemaker, M. The Electronic Structure and Ionic Diffusion of Nanoscale LiTiO2 Anatase. *Phys. Chem. Chem. Phys.* **2009**, *11*, 5742–5748. [CrossRef]